# Formation of columnar lamellar colony grain structure in a high Nb-TiAl alloy by electron beam melting

W. Kan[a], B. Chen[b,c], H. Peng[d,e*], Y. Liang[a], J. Lin[a*]

[a]*State Key Laboratory for Advanced Metals and Materials, University of Science and Technology Beijing, Beijing 100083, China*

[b]*Department of Engineering, University of Leicester, Leicester, LE1 7RH, UK*

[c]*The Institute for Advanced Manufacturing and Engineering, Coventry University, Coventry, CV6 5LZ, UK*

[d]*Key Laboratory of High-Temperature Structural Materials &Coatings Technology, Ministry of Industry and Information Technology, Beihang University, Beijing 100191, China*

[e]*School of Materials Science and Engineering, Beihang University, Beijing 100191, China*

*Corresponding authors. E-mail address: penghui@buaa.edu.cn, linjunpin@ustb.edu.cn

## Abstract

The grain morphology and texture control in electron beam melted (EBM) Ti-47Al-8Nb γ-TiAl alloy is considered. The EBM process window to obtain a columnar lamellar colony (CLC) grain structure was defined following a critical assessment of thermal gradient and liquid-solid interface velocity by using numerical simulation. Experimentally, an epitaxial grain growth during solidification of Ti-47Al-8Nb has been realised by using the optimum EBM parameter sets. The length of the CLC grain structure reached up to ~600 μm (compared to the powder layer thickness of 70 μm). The texture analysis and phase identification performed using electron backscatter diffraction (EBSD) provided important insights in understanding the solidification and phase transformation processes during the EBM fabrication. It was found that the solidification path for EBM high Nb-TiAl alloy involves the high-temperature α-phase field (i.e. L+β→α and α→$\alpha_2$+γ phase transformation processes). The epitaxial growth of prior β grains and the anchoring effect of residual B2-phase are very likely to be responsible for the formation of CLC microstructure.

**Keywords:** Solidification, Microstructure, Finite element modelling, Titanium aluminides, Electron beam melting

## 1. Introduction

The microstructure formation during the melting and subsequent solidification in electron beam melting (EBM) is known to occur far from thermodynamic equilibrium condition [1] and the final microstructure in as-EBM state is affected significantly by the complex temperature history that depends on the specific process parameter sets [2]. By manipulating the melt strategy and process parameters, the grain morphology and crystallographic texture can be controlled to promote either a columnar or equiaxed grain structure in Ni-base superalloys [3–5]. A numerical model was developed by Helmer et al. [4] and applied to understand the mechanisms for grain structure evolution in EBM IN718. It was found that columnar grain structure developed when the thermal gradient aligned with the build direction. Raghavan et al. [3] studied numerically the spatial and temporal changes of the thermal gradient and velocity of the solidification front for a point EBM melt strategy. The results were validated experimentally, proving that the location-specific grain morphology and crystallographic texture tailoring can be achieved for EBM IN718 [3].

Limited studies are available in the literature reporting the grain morphology and texture control for EBM Ti-6Al-4V and other Ti alloys (e.g. γ-TiAl intermetallic alloys, the focus of the present work). The microstructure of as-EBM Ti-6Al-4V were almost exclusively characterised by the presence of columnar prior β grains and their length was much higher than the layer thickness [6–9]. Al-Bermani et al. [6] commented that the columnar grain structure in as-EBM Ti-6Al-4V is a consequence of the thermal gradient aligned close to the build direction. Antonysamy et al. [7] performed a thorough electron backscatter diffraction (EBSD) study to clarify the β grain structure and texture formation in EBM Ti-6Al-4V. It was concluded that the comet-shaped melt pool and the beam raster direction rotation by 90° between layers, on average led to preferential growth of $<001>_{\beta}$ grains along the build direction.

A number of EBM work [10–16] were performed to produce γ-TiAl samples with the fully dense microstructure. A lamellar $\gamma/\alpha_2$ microstructure in Ti-47Al-2Cr-2Nb (all in at.% unless stated otherwise) was reported in [10]. Murr et al. [11] performed a more detailed microstructural characterisation on as-EBM Ti-47Al-2Cr-2Nb and a duplex microstructure consisting of both lamellar colony grains and equiaxed γ grains was found. The work by Biamino et al. [12,13] focused on EBM

fabrication of γ-TiAl samples and prototype. Both the Al loss and impurity elements (e.g. O and N) pick-up were very limited and with the post-processing hot-isostatic-pressing (HIP), the residual porosity can be reduced to less than 1%. When subjecting the EBM+HIP condition to a further heat treatment, various characteristic microstructures that include duplex, near-lamellar, and fully-lamellar grains can be obtained [13]. The work on EBM Ti-48Al-2Cr-2Ni [16] showed that a wide range of microstructures from equiaxed γ grains to fully-lamellar $\gamma/\alpha_2$ colony grains can be obtained in as-EBM condition by controlling the beam parameters. This conclusion has been further substantiated by the work on EBM Ti-45Al-8Nb alloy [15], where the process window was broadened by using stronger pre-heat beam current to create various characteristic microstructures in as-EBM condition.

Contrary to the commonly observed columnar grain structure in EBM Ti-6Al-4V, the presence of equiaxed grain structure in EBM γ-TiAl alloys was initially reported by Murr et al. [11], subsequently confirmed by Schwerdtfeger and Korner [16] on Ti-48Al-2Cr-2Ni and Kan et al. [15] on Ti-45Al-8Nb. There was clear evidence in [16] to show that the last deposited layer grew epitaxially from the already solidified material. However, when the sample was exposed to successive heat treatments by the deposition of subsequent layers, such a columnar grain structure was erased due to solid-state phase transformations by cyclic heat treating the material within the single α-phase region [1,16]. Important to note, Xu et al. [17] reported that equiaxed β grains in selective laser melted Ti-6Al-4V can be realised by controlling the thermal gradient within the melt pool. Our research hypothesis is thereby that a tight control on process parameters holds the promise for the columnar grain formation in EBM γ-TiAl.

By carefully investigating literature about microstructure selection for epitaxial deposition (e.g. [18]), we realise that the melt pool shape is a function of energy input, and its magnitude depends not only on the heat source power and speed but also on the thermal conductivity of the material. For Ti-6Al-4V and IN718, the thermal conductivity are 27.6 W/(mK) [19] and 29.0 W/(mK) [3] respectively, whereas the thermal conductivity for γ-TiAl alloy was calculated to be 41.2 W/(mK) by using Pandat software. Thus, the thermal conductivity of γ-TiAl is much higher than the other two, suggesting that the intrinsic tendency to form equiaxed grains is greater for EBM γ-TiAl.

In this work, we first determine the optimum combination of thermal gradient, $G$, and velocity of the solidification front, $v$, for promoting epitaxial growth in EBM Ti-47Al-8Nb. The spatial variations of $G$ and $v$ at liquid-solid interface as well as the melt pool shape were evaluated as a function of beam current and scanning speed using a stationary numerical thermal model. We then present experimental validation in terms of creating a novel columnar lamellar colony structured Ti-47Al-8Nb by using EBM. Hereafter we name this characteristic microstructure as columnar lamellar colony (CLC). Since this is the first report on CLC microstructure in EBM γ-TiAl, we also created previously reported layered microstructure [14] and homogeneous microstructure [15,16] for a comparison purpose. The crystallographic texture analysis and phase identification were performed to provide fundamental understanding of the solidification and phase transformation processes (e.g. L+β→α and α→$\alpha_2$+γ) by primarily analysing the orientation relationship.

## 2. Numerical modelling

### 2.1. A steady state process model set-up

To search for the EBM process window to create the CLC microstructure in Ti-47Al-8Nb, it is important to consider both the thermal and fluid dynamics aspects through modelling. During EBM fabrication, the melting and solidification process is continuous, hence a steady-state process model was established by using Comsol Version 5.2, Heat Transfer Module [20] to obtain the temperature distribution. Fig. 1a presents the rectangular model with dimensions of 5 × 0.6 × 0.6 $mm^3$ for the length, width and height, respectively. The analytical heat source model was based on the conjugate heat transfer model to simulate a Gaussian heat source traversing the top surface with a constant speed $v_b$. Instead of moving the heat source (i.e. electron beam) atop the rectangular model, a moving coordinate system was located at the centre of the heat source, as illustrated in Fig. 1c, and a translational motion to the opposite direction with a constant speed of $v_b$ was set. By using the coordinate system transformation, it became possible to employ refined meshes around a fixed melt pool location so that the steep thermal gradient can be solved more efficiently.

The adaptive mesh refinement was applied based on the location-specific thermal gradient, as shown in Fig. 1d. Very-fine meshes were applied to solve the

steep temperature field at and close to the melt pool, but less number of elements were used for the regions away from the melt pool. This led to the total number of elements reaching over 700,000 after at least five refinement iterations. The time required for each simulation per parameter set was approx. 4 h. It is also worthwhile to note that only one scan line was considered because the primary goal was to extract thermal gradient and velocity of the melt pool. The effect of the neighbouring scan lines on the solid-state phase transformation of a high Nb-TiAl together with the time-dependent temperature field has been reported in our previous work [15].

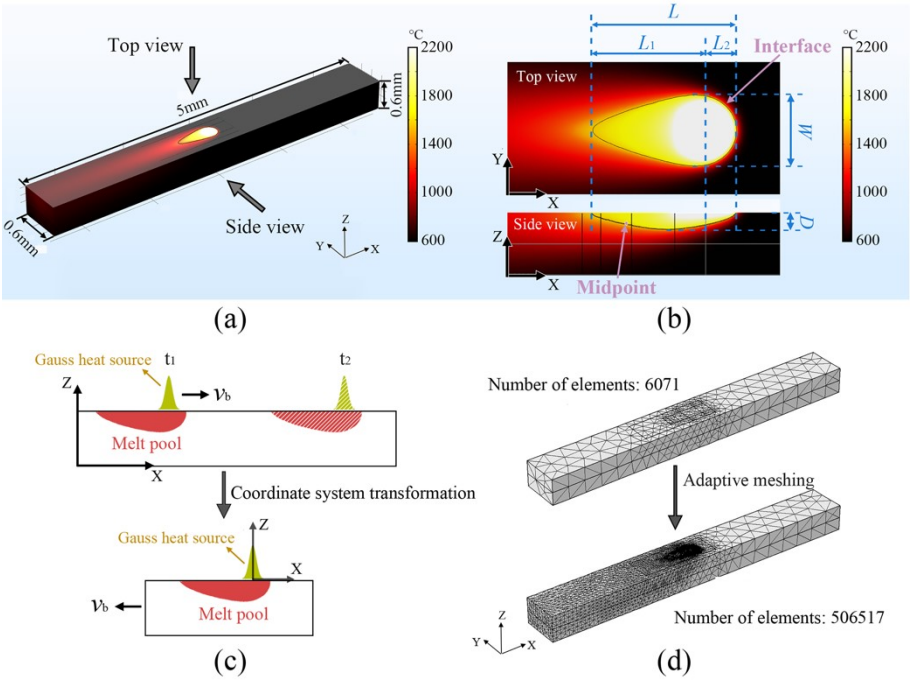


**Fig. 1.** Schematic of the simulation model to simulate the steady-state EBM process: (a) a typical temperature distribution, (b) the melt pool shape viewed from the top and side, and (c) the coordinate system transformation and (d) the adaptive meshing process for mesh refinement.

## 2.2. Governing equations for thermal and fluid dynamics

Heat conduction, convection and radiation occurred from the top surface area as indicated in Fig. 1a can be expressed by the heat transfer boundary condition:

$$-\kappa\frac{\partial T}{\partial z} = q_{\text{beam}} - h_{\text{c}}(T - T_{\infty}) - \varepsilon\sigma_{\text{e}}(T^4 - T_{\infty}^4) \tag{1}$$

where $q_{\text{beam}}$ is electron beam energy input, $h_{\text{c}}$ is the convective heat-transfer coefficient, $\sigma_{\text{e}}$ is the Stefan-Boltzmann constant, and $\varepsilon$ is radiation emissivity. $T_{\infty}$ is

room temperature and was set to 30 °C. $\kappa$ is thermal conductivity of Ti-47Al-8Nb. Electron beam as the heat source was modelled with a Gaussian distribution of beam intensity and details can be found elsewhere [15]. The initial temperature for the model simulation was set to be 1150 °C to reflect the pre-heat temperature used in the present EBM experiments. The temperature field distribution obeys the heat equation:

$$\nabla^2 T = \frac{\rho C}{\kappa}\frac{\partial T}{\partial t} \tag{2}$$

where ∇ is the Laplace differential operator for the coordinate system (x, y and z directions), $\rho$ is the density, $C$ is the specific heat capacity. This equation depicts the temperature distribution at a given location over time. The steady-state condition was granted as the time-dependent temperature variation in the overall model, $\frac{\partial T}{\partial t} \ll 10^{-5}$ °C/s was met. Note the distinct features in the present model as opposed to our previous one [15] are the fluid dynamics as well as the liquid-solid interface motion.

To model the liquid-solid phase transition by a moving boundary interface, liquid and solid parts were solved in separate domains that share a moving solidification front. In the liquid part, the thermal gradient would drive liquid-phase motion by a natural convection mechanism. This in turn affects the heat flow and liquid-solid interface (also called solidification front) displacement. The local velocity of viscous fluid is governed by the Navier-Stoke equations in the Boussinesq approximation. The flow velocity, $u$, is thus expressed by:

$$\rho\frac{\partial u}{\partial t} + \rho(u\cdot\nabla)u = -\nabla p + \mu\nabla\left(\nabla u + (\nabla u)^T\right) + \rho g \tag{3}$$

where $\rho$ is the density of viscous fluid and its magnitude depends on the temperature. $p$ is the pressure and $g$ is the standard gravity of 9.81 m/s$^2$. $\mu$ is the viscosity of the fluid and its magnitude was set as 0.05 mPa s.

With the motion of liquid-solid interface, the energy balance at the solidification front can be expressed by:

$$v_n = \frac{\Phi_l - \Phi_s}{\rho\Delta H} \tag{4}$$

where $v_n$ is the normal component of the velocity of solidification front, and $\Delta H$ is the latent heat that its value was 650 kJ/kg. $\Phi_l$ and $\Phi_s$ are the heat fluxes travelling from the liquid and solid sides respectively with their directions perpendicular to the solidification front plane. Most of the thermo-physical material properties have been tabulated in [15], and some key model inputs are given in Table 1.

**Table 1.** Thermo-physical material properties of TiAl alloy used in the simulation

| Properties | Value | Unit |
|---|---|---|
| Convective heat-transfer coefficient, $h_c$ | 80 | W/(m$^2$ K) |
| Density, $\rho$ | 2920 ~ 3250 | kg/m$^3$ |
| Latent heat, $\Delta H$ | 650 | kJ/kg |
| Radiation emissivity, $\varepsilon$ | 0.36 | N/A |
| Stefan-Boltzmann constant, $\sigma_e$ | $5.78\times10^{-8}$ | W/(m$^2$ K$^4$) |
| Specific heat capacity, $C$ | 709 ~ 789 | J/kg K |
| Thermal conductivity, $\kappa$ | 7.76 ~ 42.54 | W/(m K) |
| Viscosity, $\mu$ | 0.05 | mPa s |

## 3. Model outputs and theoretical analysis

### 3.1. Melt pool shape

Fig. 1b illustrates the top view (X-Y plane) and side view (X-Z plane) for a simulated melt pool on which the definition of melt pool length, $L$, depth, $D$, as well as width, $W$, are indicated. In terms of the melt pool length $L$, it can be further divided into two parts: the front end, $L_1$, and the back end, $L_2$, of the melt pool (both starting from the heat source centre), corresponding to the melting front and solidification front respectively. By simulating a range of beam current, $I$ (from 1 to 20 mA), and scanning speed, $v_b$ (from 1000 to 10000 mm/s), their individual and combined effects on the melt pool shape can be assessed. Here we use line energy $E_L$ as opposed to area energy to combine beam current and scanning speed ($E_L=UI/v_b$, where $U$ is the accelerating voltage of 60 kV), since a fixed value of 100 μm for the beam line offset was used.

Fig. 2a shows that the overall length of the melt pool $L$ increased with the increasing beam current $I$, while the effect of scanning speed $v_b$ on $L$ is less clear at first glance. For example, a low $v_b$ of 1000 mm/s together with a smaller beam current of 1 mA led to a greater melt pool length, however an opposite trend was

found for a higher beam current of 20 mA, Fig. 2a. To reconcile this phenomenon, Fig. 2b to 2d present the effects of $v_b$ on the total length $L$, the front end $L_1$ and the back end $L_2$ at three individual values of beam current, $I$=5 mA, $I$=10 mA and $I$=20 mA, respectively. It can be seen that $L_1$ decreased but $L_2$ increased with the increasing $v_b$. This applies for all three considered beam current values. Because of this opposite effect of $v_b$ on $L_1$ and $L_2$, the total melt pool length $L$ increased initially with the increasing $v_b$, then approached to a constant value or even started decreasing when $v_b$ became very high. This ultimately led to a fact that the maximum value of $L$ was obtained in a moderate value of $v_b$ and the maximum point shifted towards the higher $v_b$ with the increase in beam current $I$. For example, the maximum total length $L$ of 310 µm was found for $v_b$ close to 3000 mm/s (Fig. 2b), but the maximum $L$ of 351 µm was found for $v_b$ close to 4000 mm/s (Fig. 2c). It is worth noting that $L_2$ is more important compared to $L_1$ in terms of affecting the resulting solidification microstructure as that represents part of the solidification front morphology.

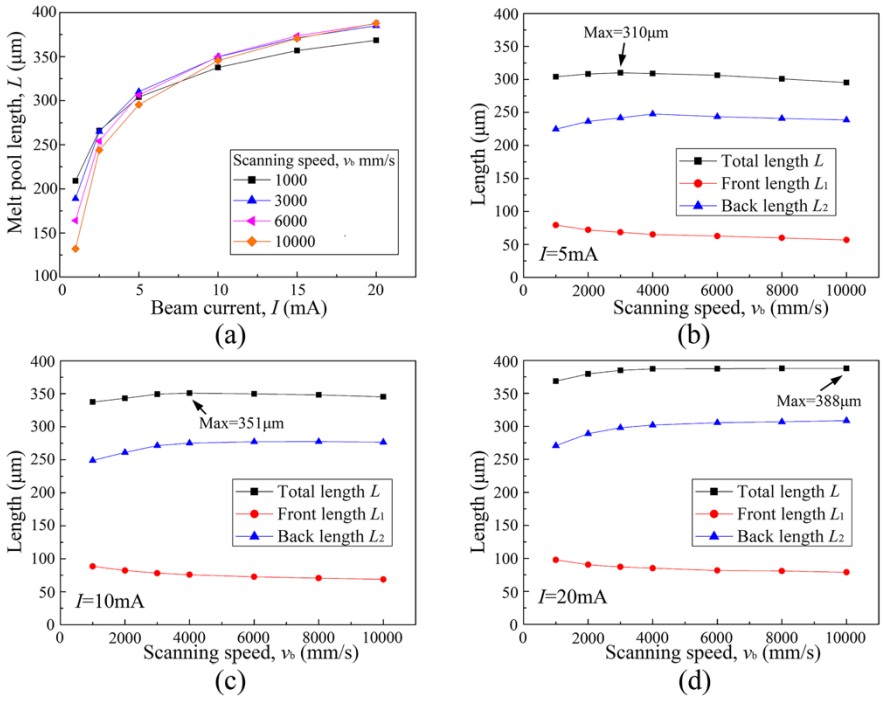


**Fig. 2.** The influence of EBM process parameters on the length of melt pool obtained by simulations: (a) changes in the total length $L$ for a range of $v_b$ and $I$, (b) to (d) changes in the total length $L$, melting front length $L_1$ and the solidification front length $L_2$ due to $v_b$ at $I$=5 mA in (b), $I$=10 mA in (c), and $I$=20 mA in (d). Note: only selected simulation data are presented in (a) to ensure figure clarity.

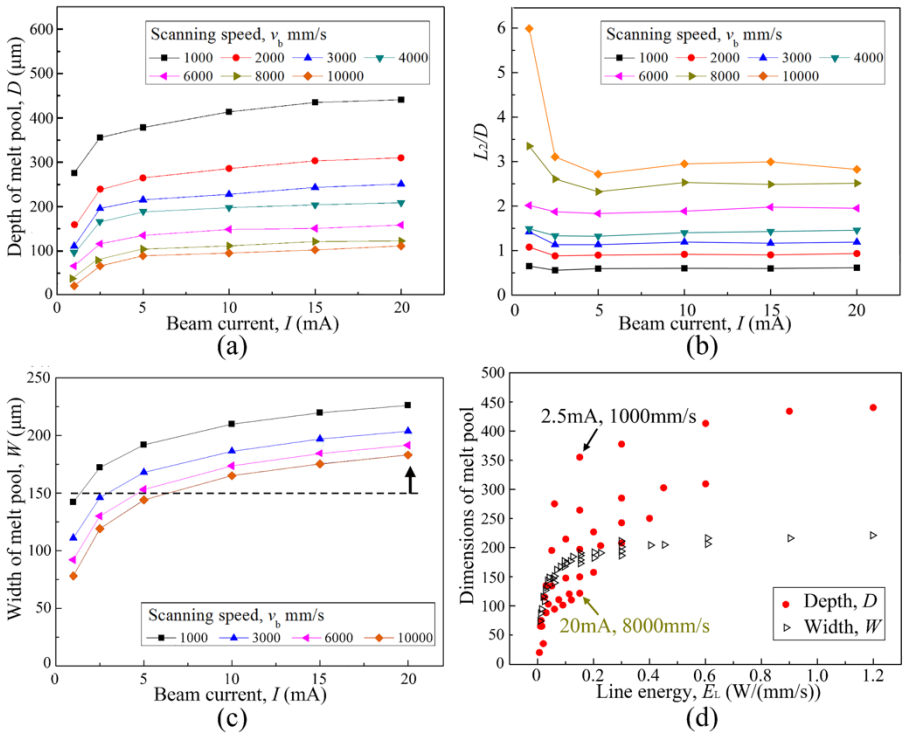


**Fig. 3.** The influence of EBM process parameters on the depth and width of melt pool obtained by simulations: (a) melt pool depth $D$, (b) the ratio of solidification front length and depth $L_2/D$, (c) melt pool depth $W$, (d) $D$ and $W$ as a function of line energy that combines both beam current $I$ and scanning speed $v_b$. Note: only selected simulation data are presented in (c) to ensure figure clarity.

Fig. 3a shows the effect of EBM process parameters on the melt pool depth $D$. It can be seen that $D$ increased monotonically with the increasing beam current $I$, but decreased with the increasing scanning speed $v_b$. It is the value of $L_2/D$ that determines the shape of the melt pool, i.e. either a spherical or comet-shaped solidification front. Hence, Fig. 3b presents their values as a function of $I$ for different $v_b$. It can be seen that the value of $L_2/D$ increased with the increasing $v_b$, suggesting that a higher scanning speed promotes a comet-shaped melt pool. It is interesting to note that the ratio of $L_2/D$ was affected less significantly by the beam current $I$, Fig. 3b.

The melt pool width is also an important factor influencing both the solidification microstructure and the relative density of the final part in as-EBM condition [21]. The change of the melt pool width $W$ is illustrated in Fig. 3c. It was found that $W$ increased with increasing $I$ but its magnitude decreased with increasing $v_b$. To obtain a fully dense microstructure in as-EBM state, a sufficient overlap between the two neighbouring scan lines is required; a rule-of-thumb value was given as 25% [22,23]. This indicates that for the scan line offset of 100 μm, the melt pool

width $W$ needs to be greater than 150 μm, as indicated in Fig. 3c. Line energy $E_L$ represents a combined effect of $I$ and $v_b$; Fig. 3d shows the change of the melt pool width $W$ and depth $D$ as a function of $E_L$. It is evident that $W$ increased with the increasing $E_L$, but $D$ did not correlate well with the $E_L$ value although broadly exhibiting an increasing trend. This means that one can control the melt pool width and depth separately under different beam parameter sets. As indicated in Fig. 3d, a similar melt pool width $W$ can be obtained at $E_L$=0.15 W/(mm/s), but the beam current $I$ and scanning speed $v_b$ can be varied proportionally to provide a very different melt pool depth $D$.

3.2. Thermal gradient and liquid-solid interface velocity

Fig. 1b outlines the melt pool boundary from which the thermal gradient $G$ at the solid-liquid interface was calculated:

$$G = \sqrt{G_x^2 + G_y^2 + G_z^2} \tag{5}$$

where $G_x$, $G_y$ and $G_z$ are the thermal gradients at the solid-liquid interface along X, Y and Z directions, respectively. Their values were extracted by a probe from the midpoint of the solidification front as indicated in the X-Z plane of Fig. 1b. The midpoint was determined as the intersection between the half of the melt pool depth and solidification front interface. Because of the dramatic change in the temperature field close to the solid-liquid interface, determination of the specific value of $G$ often came with a random error. To tackle this raw data fluctuation, the linear least square regression technique was used to determine the value of $G$. The normal component of the velocity of solid-liquid interface motion $v_n$ can be calculated by knowing the magnitude of scanning speed $v_b$ and the angle $\theta$ between these two:

$$v_n = v_b \cdot \sin\theta = v_b \cdot \frac{G_x}{\sqrt{G_x^2 + G_y^2 + G_z^2}} \tag{6}$$

Fig. 4a shows the change of $G_z/G_x$ for a range of beam current $I$ and scanning speed $v_b$. A higher value of $G_z/G_x$ can be obtained with the increase in $v_b$, and the effect of $I$ became noticeable only for the higher values of $v_b$. It is shown in Fig. 4a

that, a very high $G_z/G_x$ of being greater than 10 can be obtained when $v_b$ is greater than 4000 mm/s. This indicates that under theses beam conditions, it is likely to promote the epitaxial grain growth along the build direction (Z-direction). Furthermore, the dependencies of $G_z/G_x$ on beam current $I$ and scanning speed $v_b$, Fig. 4a, are similar to what have been observed for $L_2/D$, Fig. 3b. This confirms that a comet-shaped melt pool often results in a higher ratio of $G_z/G_x$. Fig. 4b presents the ratio of thermal gradient and velocity, $G/v_n$, that determines the mode of solidification (i.e. a columnar or equiaxed grain structure). The values of $G/v_n$ for the considered parameter sets ranged from $3.3\times10^7$ to $1.0\times10^{10}$ K s/m$^2$. It can be seen in Fig. 4b that the $G/v_n$ value increased markedly with $I$, but the effect of $v_b$ on $G/v_n$ exhibiting an initial increase and then decrease with the increasing $v_b$. The maximum values of $G/v_n$ were obtained with a moderate scanning speed $v_b$ of between 4000 and 8000 mm/s together with the high beam current values of between 15 and 20 mA, see the shaded box in Fig. 4b. Within these parameter sets, it is reasonable to postulate that a relatively higher scanning speed $v_b$ would help to promote the epitaxial growth of grains with their major axis aligning with the build Z-direction as the ratio of $G_z/G_x$ increased monotonically with the increasing $v_b$, as highlighted in Fig. 4a. Experimental validation about the formation of columnar lamellar colony (CLC) grain structure in EBM Ti-47Al-8Nb is presented in the following sections.

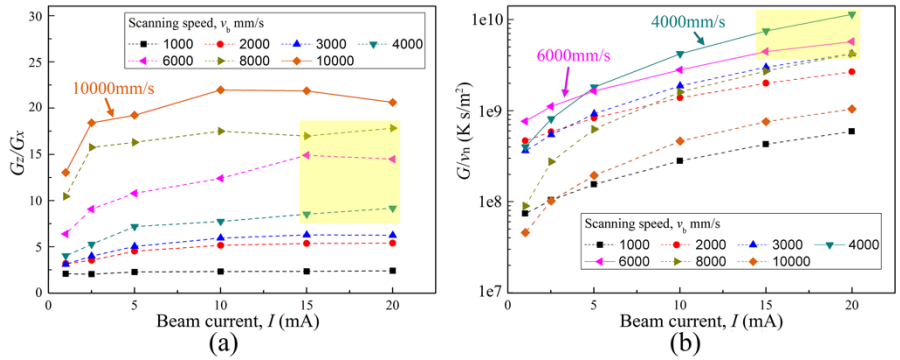


**Fig. 4.** The influence of beam current $I$ and scanning speed $v_b$ on directionality of thermal gradient $G_z/G_x$ in (a) and the ratio of thermal gradient and velocity, $G/v_n$ in (b). The shaded areas in (a) and (b) highlights the recommended process window for promoting the epitaxial grain growth in EBM γ-TiAl alloy.

## 4. Experimental validation

To validate simulation results, EBM samples with dimensions of 30 × 30 × 30 mm$^3$ consisting of more than 400 powder layers were fabricated using an Arcam

A2XX machine with Control Software 3.2 in the manual mode. Rapidly solidified pre-alloyed Ti-47Al-8Nb powders were used for the EBM fabrication and these powders were produced by plasma melting inert gas atomisation. The pre-heat beam parameters were the same for all samples, leading to a build temperature of 1150 °C. A standard line scan melt strategy was used with a powder layer thickness of 70 μm. A line offset $L_{off}$ of 100 μm was used. More detailed description about EBM sample fabrication can be found elsewhere [5,15]. Totally three typical characteristic microstructures were created using a range of beam current $I$ and scanning speed $v_b$; these parameter sets are presented in Table 2 together with the calculated line energy $E_L$. The CLC (columnar lamellar colony) epitaxial grain structure is the newly discovered microstructure in EBM γ-TiAl (sample A in Table 2), compared to the other two: the homogeneous microstructure characterised by the near-equiaxed grains for samples B and C, and the layered microstructure characterised by alternating layers of duplex-phase region and γ-grain band for sample D.

**Table 2.** Summary of EBM process parameter sets selected for evaluating characteristic microstructures in Ti-47Al-8Nb.

| Sample ID (microstructure acronym) | Melting parameter sets | | | Density. % |
|---|---|---|---|---|
| | Beam current, mA | Scanning speed, mm/s | Line energy, W/(mm/s) | |
| A (CLC) | 20.0 | 6000 | 0.20 | 99.6 |
| B (Homogeneous) | 20.0 | 3500 | 0.34 | 99.3 |
| C (Homogeneous) | 7.0 | 2200 | 0.19 | 99.6 |
| D (Layered) | 17.5 | 6000 | 0.175 | 99.8 |

The chemical compositions of both the virgin powders as well as the as-EBM samples were analysed by inductively coupled plasma atomic emission spectroscopy (ICP-AES). A Carl Zeiss Supra 40 VP field emission scanning electron microscopy (SEM) equipped with EBSD detector was used to characterise the microstructures in the as-EBM samples. All the metallographic specimens were extracted from a similar sample height position of 5 to 7 mm below the top surface for a comparison purpose (samples A to D in Table 2). The vertical cross-sectional plane (X-Z plane) was then ground, mechanically polished and finally electrolytically polished using a chemical solution (5% perchloric acid + 30% butanol + 65% methanol). Most of the SEM images were taken using BSE mode to enhance the contrast of the microstructural features. EBSD was used for identifying crystallographic orientation and generating phase constitution maps. An accelerating voltage of 20 kV in a high current mode

and an aperture size of 120 μm were used to maximise the signal-to-noise ratio. EBSD maps were collected with a step size of 1 μm and data analysis was performed using HKL Channel 5 software from Oxford Instruments. In addition, X-ray diffraction (XRD) phase identification was performed with a Bruker D8 Advance with Cu Kα diffraction.

## 5. Results and discussion

### 5.1. Columnar lamellar colony grain structure in EBM Ti-47Al-8Nb

Fig. 5a shows the microstructure of sample A (X-Z plane), that was fabricated with the beam current of $I$=20 mA and scanning speed of $v_b$=6000 mm/s, Table 2. The microstructure of sample A is characterised by large elongated prior β-phase columnar grains that have developed epitaxially from the bottom to the top of EBM build, i.e. more or less parallel to the build direction, Fig. 5a. Within each columnar grain, lamellar colonies with different orientations relative to the Z-direction can be seen in Fig. 5a. The inset in Fig. 5a illustrates the characteristic lamellar structure. It is important to note that such a columnar lamellar colony (CLC) microstructure in EBM γ-TiAl alloys has not been reported previously. To substantiate this CLC microstructure, different EBM beam parameters were applied to create homogenous and layered microstructures typical of those already revealed for various EBM γ-TiAl alloys [14–16] but not for Ti-47Al-8Nb. Sample B shows a characteristic microstructure of equiaxed γ grains (Fig. 5b), while sample C exhibits a near-lamellar microstructure with obvious microstructural degradation as described in [28] (Fig. 5c). Both belong to the homogenous microstructure group as opposed to sample D exhibiting a layered microstructure that consists of alternating duplex phase region and elongated γ bands, Fig. 5d. It is also important to note that all EBM samples A to D had a fully-dense microstructure and the measured relative density was above 99% (Table 2).

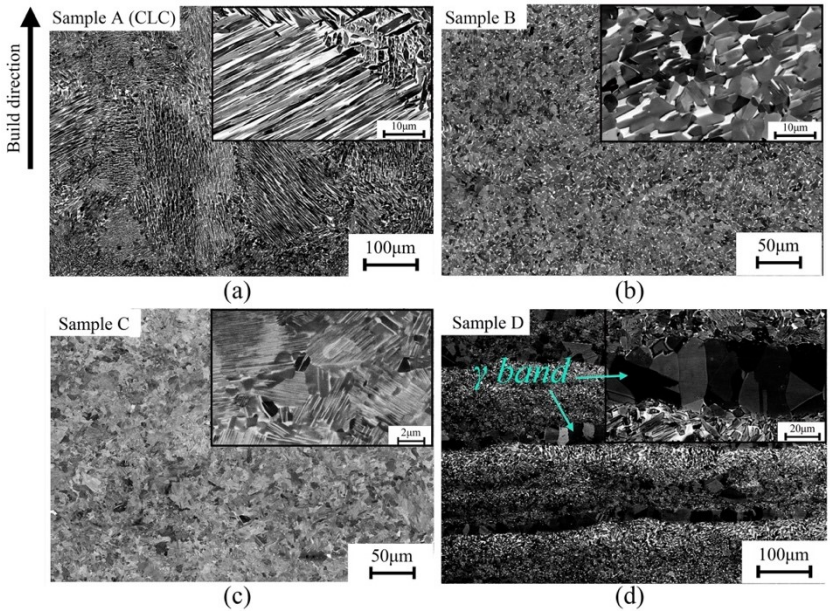


**Fig. 5.** SEM micrographs (X-Z plane view): (a) sample A with the columnar lamellar colony (CLC) grain structure; (b) sample B with the equiaxed γ grain structure; (c) sample C with near-lamellar equiaxed grain structure; (d) sample D with the layered microstructure consisting of alternating layers of duplex-phase region and elongated γ-phase bands. Note: insets shows microstructural features in detail.

5.2. Phase identification and texture analysis

The selected area as outlined by red colour in Fig. 6a represents one particular columnar lamellar colony grain whose length reaches approx. 600 μm along the build direction, equivalent to 9 to 10 powder layers. The lamellar orientations maintain the same within one particular colony. Fig. 6b and 6c are the corresponding EBSD IPF orientation maps for γ and B2 phases respectively. Note B2-phase is the room-temperature ordered β-phase for TiAl intermetallic alloy. From the IPF colouring EBSD map for γ-phase, Fig. 6b, it can be seen that the lamellar structure primarily contains two sets of γ-phase lamellae with distinct orientations. In terms of the B2-phase as shown in Fig. 6c, the prior β columnar grain structure can be easily identified by their relative orientations. In addition, each prior β columnar grain consists of several extended lamellar colonies, see Fig. 6a to Fig. 6c for the green coloured columnar grain. This indicates that these individual γ/B2 lamellar colonies might originate from the same parent β columnar grain. In other words, upon cooling, it is likely that the transformed γ-phase obeys a strong orientation relationship with the parent β-phase.

A selected area as outlined by the white box in Fig. 6a to 6c includes one particular lamellar colony grain. The corresponding pole figures are shown in Fig. 6d for γ-phase and Fig. 6e for B2-phase. Fig. 6d shows two γ-phase variants, represented by green and purple colours respectively, and they are superimposed on the position indicated by the violet coloured arrow. Fig. 6e shows the pole figure for B2-phase; the majority of B2-phase has a $<101>_{\beta}$ orientation and the B2-phase is found to be located at the same positon as indicated by the violet arrow. This means that the two γ-phase variants in one particular lamellar colony grain shares the same orientation relationship with B2-phase as $\{111\}_{\gamma}\|\{110\}_{\beta}$. It is important to note that the γ/B2 lamellar structure is present for the CLC microstructure; this is quite different to the previous work where a $\gamma/\alpha_2$ lamellar structure was found in EBM γ-TiAl alloys [11,14–16]. The appearance of γ/B2 lamellar structure is not only related to the thermal history determined by the melt parameters, but also affected by the change in equilibrium phase constitution caused by the Al loss. Detailed texture analysis and solidification path as well as phase transformations for sample A with CLC microstructure will be given in section 5.3.

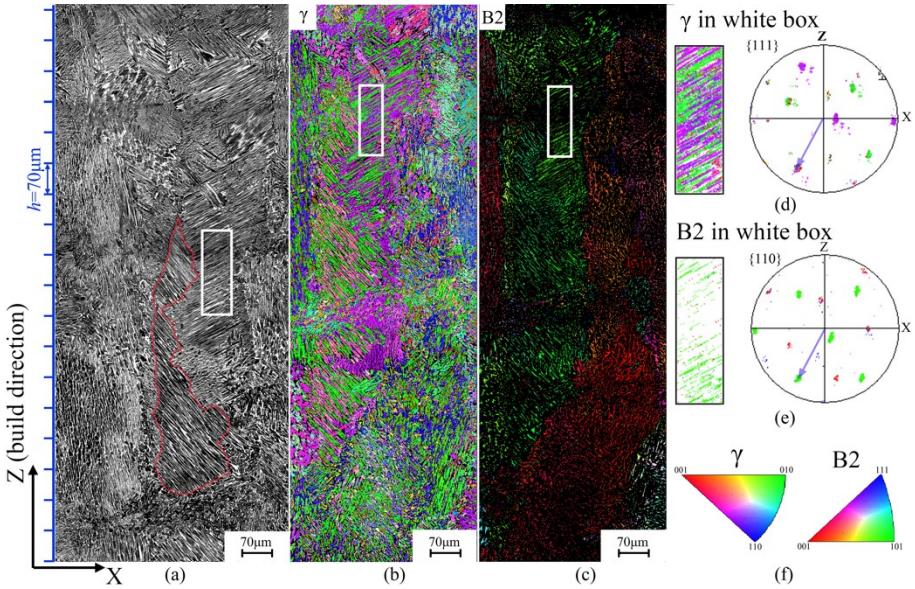


**Fig. 6.** EBSD analysis of sample A: (a) BSE micrograph; (b) and (c) IPF orientation maps for the indexed γ and B2 phases respectively; (d) and (e) pole figures for the white box region illustrating the orientation relationship of γ and B2 phases; (f) IPF colour key.

In terms of samples B and C (Table 2) with the homogeneous microstructure, Fig. 7a and 7b show the IPF orientation maps for γ and B2 phases of samples B, while Fig. 7c and 7d for sample C. By comparison with Fig. 6c for sample A, there is very

little B2-phase remained for both samples B and C, Fig. 7b and 7d, and no such a prior β columnar grain structure can be seen. The phase constitution quantitative analysis by EBSD, summarised in Table 3, show that the percentage of B2-phase in sample A is the highest of 14.9%, followed by 7.8% for sample B, and 2.1% for sample C. In terms of the γ-phase IPF orientation maps, the lamellar colony structure as observed in Fig. 6b for sample A cannot be seen in Fig. 7a for sample B and Fig. 7c for sample C. The $<110>_{\gamma}$ pole figures (not shown here) for samples B and C show a relatively weak, 3.1 and 2.3 times random texture, when compared to sample A that shows 7.8 times random, indicating a stronger texture. In terms of the layered microstructure for sample D, the epitaxial growth should be more difficult as the blocking effect of alternating γ bands. Hence, it is not surprising to see the absence of columnar microstructure for sample D (Fig. 7e and 7f). Also can be seen in Table 3, the phase of majority in all samples A to D is γ-phase. For sample B with the equiaxed γ grain microstructure, the noticeable brighter phase located at grain boundary junctions, Fig. 5b, was identified as B2-phase.

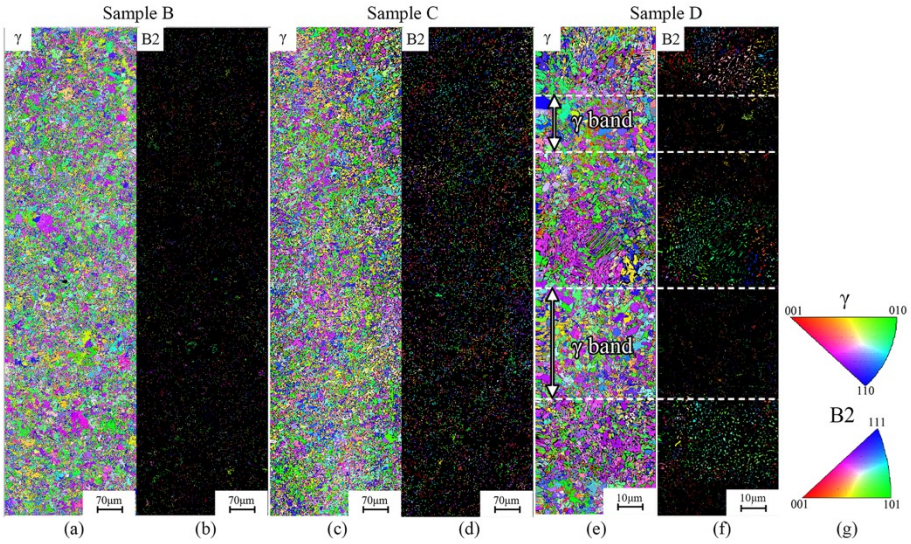


**Fig. 7.** IPF orientation maps for the indexed γ-phase in (a), (c) and (e) and B2-phase in (b), (d) and (f). (a) and (b) sample B with equiaxed γ grain structure; (c) and (d) sample C with near-lamellar equiaxed grain structure; (e) and (f) sample D with layered microstructure.

**Table 3.** EBSD determined phase constitution for samples A to D as well as the Al loss.*

| Sample ID | Microstructures observation by SEM | Phase constitution, % | | | Al loss, at.% |
|---|---|---|---|---|---|
| | | B2 | $\alpha_2$ | $\gamma$ | |
| A | Columnar $\gamma$/B2 lamellar | 14.9 | 1.1 | 84.0 | 1.4 |
| B | Equiaxed $\gamma$ grain + B2 | 7.8 | 0.4 | 91.7 | 1.8 |
| C | Equiaxed near-lamellar ($\gamma/\alpha_2$) | 2.1 | 0.4 | 97.5 | 0.7 |
| D | Layered (duplex phase + $\gamma$ bands) | 5.7 | 0.4 | 93.9 | 1.2 |

Fig. 8 shows the XRD spectra for samples A (CLC microstructure), C (homogeneous microstructure) and D (layered microstructure). It can be seen that $\gamma$-phase is the phase of majority. The characteristic peak $(002)_\beta$ for B2-phase is present for sample A with CLC microstructure and to a less extent for sample D with layered microstructure. The XRD phase constitution results are consistent with those measured by EBSD. It should be noted that the different phase constitution in samples A to D is primarily related to the different thermal histories under various EBM melt parameters (e.g. $I$ and $v_b$).

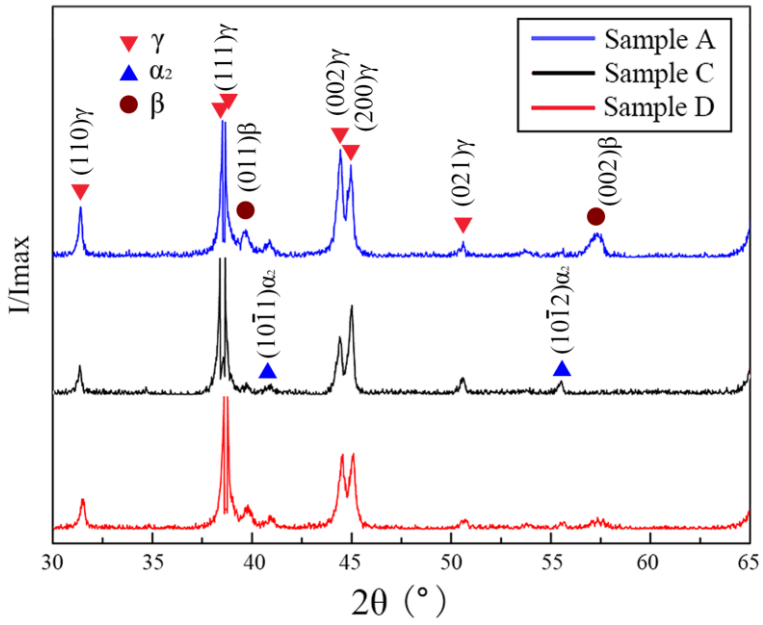


**Fig. 8.** (a) XRD spectra of samples A, C and D to indicate the phase constitution changes†

* Because of the small size of $\alpha_2$ grains comparing to the step size of EBSD detection (1μm), the low phase constitutions of $\alpha_2$ below 1.0% are only a qualitative measure rather than a precisely quantitative result.

† The diffraction peaks were normalised with respect to the characteristic peak of $(111)_\gamma$ with the highest peak intensity.

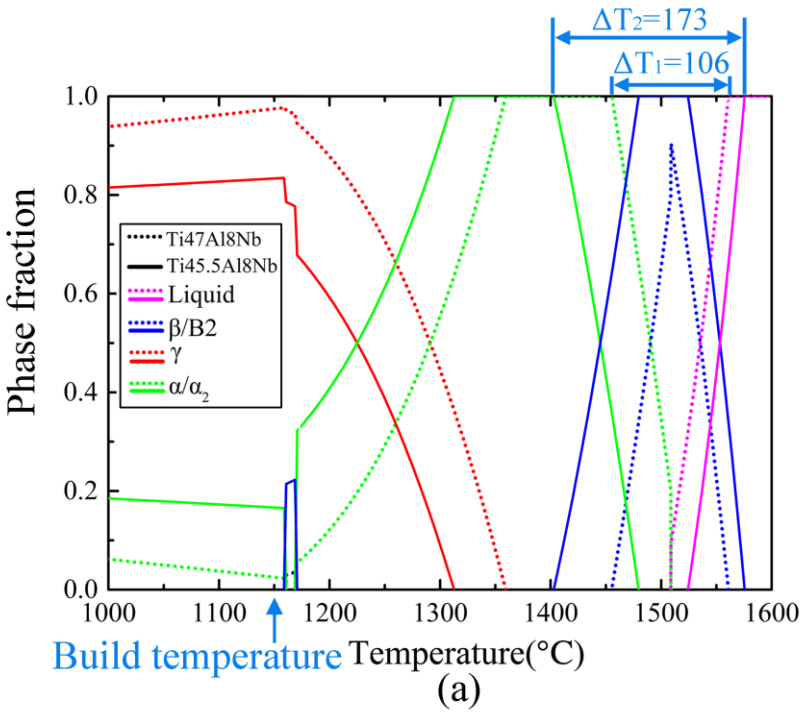


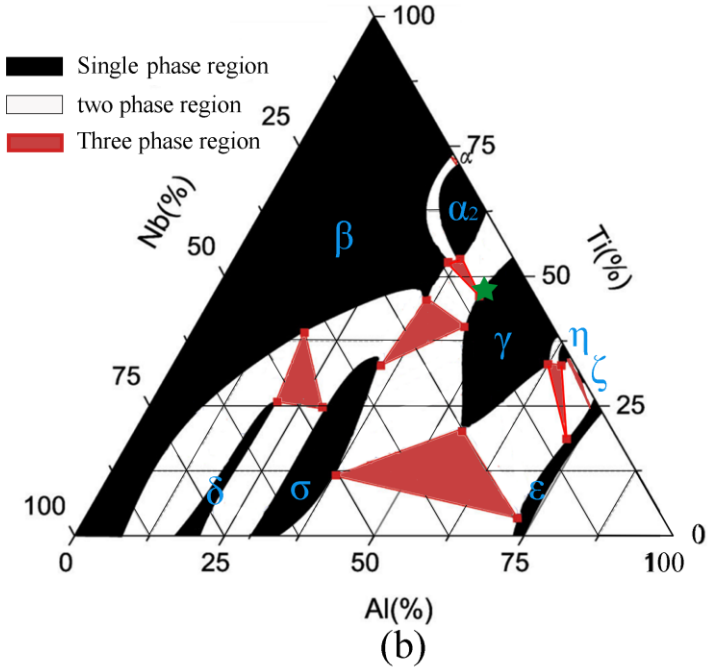


**Fig. 9.** (a) the phase composition of Ti-47Al-8Nb (dotted lines) and Ti-45.5Al-8Nb (solid lines), (b) the 1150 ℃ isothermal section of Ti-Al-Nb phase diagram in which the green star represents the chemical composition of sample A [26].

For EBM γ-TiAl alloy, Al loss can be used as one of the reasons to explain the resulting microstructure and phase constitution in as-EBM condition. The peritectic point (L+β→α) for the high Nb-TiAl alloy equilibrium phase diagram in terms of Al conent was calculated to be 47.4 to 49.2 at.% [24,25]. These calculations were based on Thermo-Calc software in a Ti-Al-Nb ternary system where Nb contents ranged

between 7 and 10 at.%. Since the Al content of the initial powder is 47 at.%, the as-EBM TiAl is judged as hypo-peritectic alloy composition as a result of the light element (e.g. Al) evaporation during EBM fabrication. Based on the optimised database of Ti-Al-Nb ternary phase diagram reported by the Witusiewicz [26], we used Pandat to calculate the phase composition of Ti-47Al-8Nb and Ti-45.5Al-8Nb under the thermodynamic equilibrium condition. As shown in Fig. 9a, the equilibrium phase constitution for Ti-47Al-8Nb at a temperature of 1150 ℃ is 97.5% (γ) and 2.5% ($\alpha_2$). In terms of sample A, because of the Al loss of 1.5%, the phase composition is 83.3% (γ) and 16.7% ($\alpha_2$), which is different from the phase constitution of 14.9% (B2), 84.0% (γ) and 1.1% ($\alpha_2$) as determined by EBSD in Table 3 for sample A. Possible explanations are discussed in detail below about the presence of a higher content of residual B2-phase and associated lower content of $\alpha_2$-phase for sample A in as-EBM condition.

The high content of residual B2-phase in sample A is mainly caused by the incomplete transition of the prior β-phase through the phase transformation of β→α during the rapid cooling process. In addition, the effect of Al loss (1.5%) on phase composition should not be neglected. In terms of the kinetic process for the phase transformation, the Al loss leads to a fact that the prior β-phase becomes more difficult to be transformed to α-phase during cooling, because the reduction in Al content in the alloy system would result in the expansion of the temperature range of β/B2 phase zone, see Fig. 9a. The temperature range of β/B2 phase zone for Ti-45.5Al-8Nb was calculated to be $\Delta T_2$=173 ℃, which is 63% higher than that for Ti-47Al-8Nb (delta $\Delta T_1$=106 ℃), in Fig. 9a. The expanded β/B2 phase zone particularly move towards a lower temperature region for Ti-45.5Al-8Nb means that the kinetic process of such a phase transformation from β→α at high temperature is more sluggish.

In terms of the thermodynamic evolution during the long-term annealing process, with the Al loss of 1.5% in sample A, the residual B2-phase becomes a stable phase in the temperature range of 1160 to 1175 °C, and its equilibrium composition can reach 20%, according to the phase constitution calculation as shown in Fig. 9a. Since the build temperature is the measured temperature at the bottom of the substrate plate, the actual annealing temperature should be slightly higher than the actually measured build temperature of 1150 °C [15]. Therefore, it is very likely that the B2-phase is a more stable phase in this temperature region. Finally, even if the annealing

temperature is not within the B2-phase region, the driving force of the phase transition from β to α and γ phases is insufficient because of the small undercooling temperature which is predicted to be less than 50 °C[‡], Fig. 9a. In sum, the effect of Al loss on both the kinetic and thermodynamic process are responsible for the resulting high amount of residual B2-phase of up to 14% for sample A, Table 3.

Now we need to discuss the discrepancy between the observed very low content of $\alpha_2$-phase and the thermodynamic calculated approx. 17% $\alpha_2$-phase at the build temperature, see Fig. 9a. Since the residual β/B2 phase is rich in Nb and lean in Al, the higher proportion of residual β/B2 phase compared to that under the equilibrium condition would result in that the remaining α/γ phase system has a less Nb but a higher Al content. As suggested by the 1150 °C isothermal section of Ti-Al-Nb phase diagram in Fig. 9b, the residual β/B2 phase (rich in Nb and lean in Al) would cause the green star move towards the low Nb and high Al content region, which makes the green star being closer or even within the γ-phase zone. This leads to a significant decrease of $\alpha_2$ phase constitution in its thermodynamic equilibrium condition.

With the reduction in Al content, an increasing amount of β-phase is formed upon cooling from the melt in sample A, when compared to those hyper-peritectic alloy (note: Nb moves the peritectic point to a higher Al content). Thus one might attempt to correlate the different B2-phase constitutions from samples A to D with the measured Al loss for the present Ti-47Al-8Nb γ-TiAl. To this end, the measured Al loss data for all samples A to D are summarised in Table 3. At first glance, the Al loss and B2-phase constitution seems to be positively correlated, i.e. the B2-phase decreased from 14.9% in sample A to 2.1% in sample C with the decreased Al loss from 1.4% to 0.7%. But this does not account for the relationship between sample A and sample B. With the increase of scanning speed $v_b$ from 3500 mm/s in sample B to 6000 mm/s in sample A (Table 2), the decreased Al loss in sample A came with an unexpected very high B2-phase content of 14.9% compared to that of 7.8% for sample B (Table 3). Although the equilibrium phase constitution can be determined by Al content for a thermodynamic equilibrium state, the actual EBM melting process

[‡] The annealing temperature is slightly higher than the build temperature (1150 °C), and the B2 phase zone is between 1150 and 1200 °C, so the undercooling temperature should be less than 50 °C.

involves a complex temperature history. This means that the resulting phase constitution is also affected by the time-dependent kinetic process.

It is important to note that the scanning speed of $v_b$=6000 mm/s in sample A is almost twice that of sample B, which leads to a significant increase in thermal effect between adjacent scanning lines. Schwerdtfeger and Korner [16] pointed out that geometric effects started to come into play for the high scanning speed as a short return time would be expected. For a short return time, the heat built up from the last scanning line is not fully dissipated when the next scanning line reaches the same location but with a line offset. The higher overall heat in sample A may lead to two possible consequences that could account for the higher B2-phase content of 14.9% in Table 3. One is the longer hold time in β-phase region of above 1500 °C, which leads to a higher amount of residual B2-phase upon cooling. The other is that the pre-solidified material might have experienced a longer time of heat treatment at temperatures of between 1150 to 1250 °C (i.e. above the build temperature of 1150 °C due to the incomplete heat dissipation). As B2-phase is the thermodynamic equilibrium phase at this temperature range [25,26], this could cause already-transformed $\alpha_2$-phase upon cooling to decompose to B2-phase due to high-temperature exposure, essentially a high-temperature degradation process. At this stage, although it is impossible to rule out one or the other, we are inclined to accept the former, because of the very significant difference of B2-phase content for sample A compared to the others, Table 3.

### 5.3. Solidification path and phase transformation

Fig. 10a shows that the B2-phase grains in sample A are highly textured with 18 and 9 times random and the preference of the $\{100\}_{B2}$ pole lies parallel with the Z-direction and within X-Y plane. This indicates the presence of epitaxially and extended growth of prior bcc-β grain along the heat flow of Z-direction. Fig. 10d shows that the poles of $\{0001\}_{\alpha 2}$ are mainly gathered at five positions represented by the white coloured arrows, all of which are able to find the superimposed position in the pole figure of $\{110\}_{B2}$ in Fig. 10b. The presence of $\{0001\}_{\alpha 2}||\{110\}_{\beta}$ in the phase transformation of L+β→α is known as Burgers orientation relationship between the β-TiAl (bcc) and α-TiAl (hcp), expressed as $\mathbf{(0001)_{\alpha 2}||\{110\}_{\beta}}$ **and** $\mathbf{<11\bar{2}0>_{\alpha 2}||<1\bar{1}1>_{\beta}}$.

The orientation relationship represented by the $\{110\}_{\gamma}$ pole figure in Fig. 10h and $\{11\bar{2}0\}_{\alpha 2}$ pole figure in Fig. 10e, indicates the presence of Blackburn relationship (i.e. $\mathbf{(111)_{\gamma}||\{0001\}_{\alpha 2}}$ **and** $\mathbf{<1\bar{1}0>_{\gamma}||<11\bar{2}0>_{\alpha 2}}$) for the solid-state phase transformation of $\alpha \rightarrow \alpha_2+\gamma$. The Blackburn relationship is always noticed between the α-TiAl (hcp) and γ-TiAl (fcc), which indicates the appearance of α/γ lamellar structure formed by eutectoid transformation during the EBM cooling (i.e. without a further microstructural degredation effect). From the texture analysis above, it is likely to conclude that both the phase transformations of $L+\beta \rightarrow \alpha$ and $\alpha \rightarrow \alpha_2+\gamma$ are responsible for the resulting phase constitution in as-EBM sample A, even though the amount of $\alpha_2$-phase was measured to be only 1.1%, Table 3. Finally, the observation of orientation relationship $\{111\}_{\gamma}||\{110\}_{\beta}$ on γ/β interface is not surprising for TiAl alloy, because the non-equilibrium α-phase formed in high cooling process is always consumed by the discontinuously coarsened γ during long-term annealing, which result in this combined orientation relationship of Burgers and Blackburn orientation relationship [27,28]. In other words, the solidification path for EBM high Nb-TiAl alloy involves the high-temperature α-phase field, rather than a direct phase transformation from $\beta \rightarrow \gamma$.

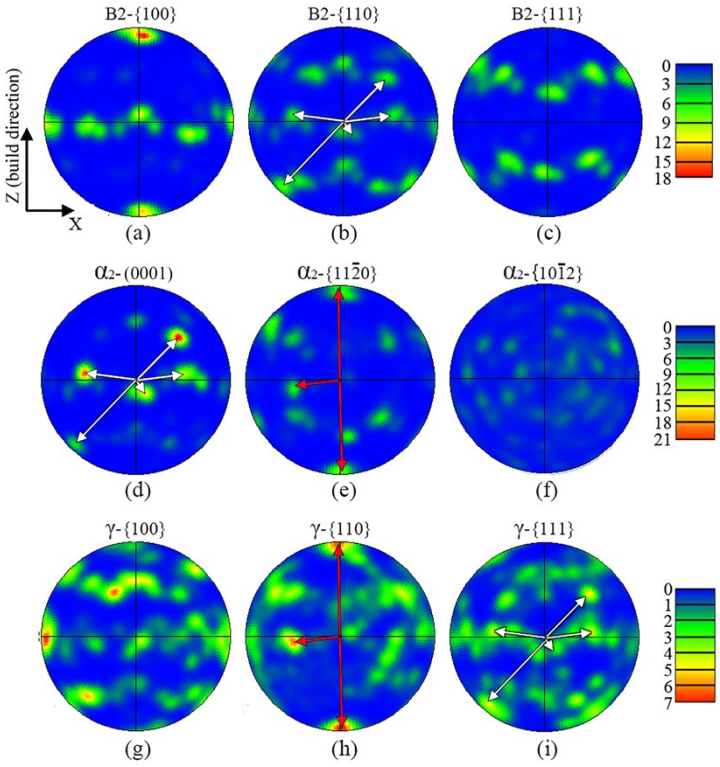


**Fig. 10.** Pole figures of B2-phase in (a) to (c) and $\alpha_2$-phase in (d) to (f) as well as γ-phase in (g) to (i). Pole figures of (a) {100}, (b) {110} and (c) {111} for B2-phase;

pole figures of (d) {0001}, (e) $\{11\bar{2}0\}$ and (f) $\{10\bar{1}2\}$ for $\alpha_2$-phase; pole figures of (g) {100}, (h) {110} and (i) {111} for γ-phase.

The orientation relationships between the prior β-phase and the nucleated α-phase, based on the Burgers orientation relationship are schematically illustrated in Fig. 11 for two variants of α-TiAl phase (hcp). This can be used to explain the formation mechanism of $<11\bar{2}0>_\alpha$ texture in Fig. 10e.

Because of the preferred growth of $[001]_\beta$ along the heat flow during the EBM solidification stage, the direction of $[001]_\beta$ is parallel to Z, and the $[100]_\beta$ and $[010]_\beta$ direction are within the X-Y plane in sample A, see the top row of three figures in Fig. 11a to 11c. This agrees very well with our EBSD pole figure for B2-phase, Fig. 10a. There are three independent crystallographic planes of type $\{110\}_\beta$, as illustrated by the blue coloured planes in the top row of Fig. 11a to 11c, from which the α-TiAl phase will nucleate and grow by aligning their $(0001)_\alpha$ basal plane with $\{110\}_\beta$ that include $(110)_\beta$, $(011)_\beta$ and $(101)_\beta$. Moreover, based on the Burgers orientation relationship (i.e. the direction of $<11\bar{2}0>_\alpha||<1\bar{1}1>_\beta$), one of the three $<11\bar{2}0>_\alpha$ directions in the $(0001)_\alpha$ plane needs to be parallel to the $<1\bar{1}1>_\beta$ direction of the original $\{110\}_\beta$ plane. Because there are two different $<1\bar{1}1>_\beta$ directions for each plane of type $\{110\}_\beta$, this means that two possible α-phase variants exist for each of prior β-phase, as highlighted by green and purple colours in the bottom row of three figures for $(110)_\beta$ in Fig. 11a, $(011)_\beta$ in Fig. 11b, and $(101)_\beta$ in Fig. 11c, respectively.

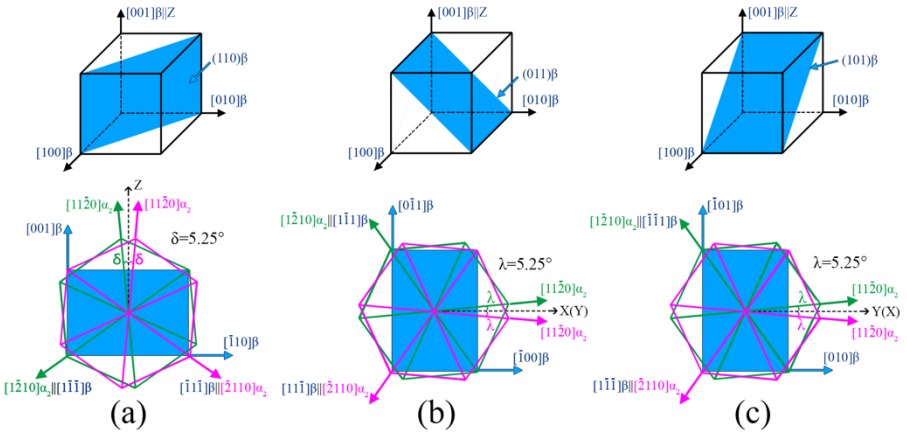


**Fig. 11.** Schematic diagrams showing two possible variants of α-TiAl phase (hcp), highlighted by green and purple hexagons, nucleated from the crystallographic planes of $(110)_\beta$, $(011)_\beta$, $(101)_\beta$ in (a) to (c), respectively. The β→α peritectic phase transformation followes the classic Burgers orientation relationship of $\{0001\}_\alpha||\{110\}_\beta$ and $<11\bar{2}0>_\alpha||<1\bar{1}1>_\beta$. Note: δ represents the angle between $[11\bar{2}0]_\alpha$ direction, while Z and λ represent the angle between $[11\bar{2}0]_\alpha$ direction and X-Y plane respectively.

Fig. 11a illustrates that two different α variants were formed based on $[1\bar{2}10]_{\alpha}||[1\bar{1}\bar{1}]_{\beta}$ and $[\bar{2}110]_{\alpha}||[\bar{1}1\bar{1}]_{\beta}$, respectively. This geometrical symmetry results in that the angle between $[11\bar{2}0]_{\alpha}$ direction and Z-direction (EBM build direction), is δ=5.25°, as indicated in Fig. 11a. Following the same geometrical symmetry (in this case $[1\bar{2}10]_{\alpha 2}||[1\bar{1}1]_{\beta}$ and $[\bar{2}110]_{\alpha 2}||[11\bar{1}]_{\beta}$), Fig. 11b show that the angle between $[11\bar{2}0]_{\alpha}$ and X-Y plane, is λ=5.25° for $(011)_{\beta}$ plane as the parent phase. Moreover, because the only restricted condition of $[100]_{\beta}$ and $[010]_{\beta}$ direction is within the X-Y plane, the $(011)_{\beta}$ and $(101)_{\beta}$ are geometrically equivalent. Hence the angle λ is also 5.25°, when α-phase transformed from $(101)_{\beta}$, as shown in Fig. 11c. From the geometrical symmetry analysis above, it is now understood that the preferred growth of $[001]_{\beta}$ along Z-direction would lead to two variants of the transformed α-phase from each parent β-phase and the product α-phase should follow such an orientation relationship of $[11\bar{2}0]_{\alpha}$ direction being almost parallel (with a deviation of 5.25°) to Z-direction or within X-Y plane. As a result, this explains the seemingly correlation between the pole figure of $\{11\bar{2}0\}_{\alpha}$ in Fig. 10e and $\{100\}_{\beta}$ in Fig. 10a.

5.4. Formation mechanisms of the columnar lamellar colony grain structure

The formation of $[001]_{B2}$ texture in sample A with CLC microstructure, Fig. 10a and Fig. 6a, evidences that it is possible to promote epitaxial growth of prior β-phase in EBM γ-TiAl, Fig. 6c, by a tight control of thermal gradient $G$ and velocity of solidification front $v$. The primary criteria for the creation of CLC microstructure are $G/v_n$ and $G_z/G_x$. Depending on the rise of the constitutional undercooling ahead of the advancing front, a higher $G/v_n$ leads to the morphology change of solidification microstructure from cellular to dendritic [18]. Based on an experimental study of directional solidification in Ti-46Al-8Nb alloy, Lapin [29] commented that a critical value of $G/v_n=1\times10^7$ K s/m$^2$ would be required to trigger the equiaxed-to-columnar transition. The present experiment-validated simulation results also highlight that a high value of $G_z/G_x>10$ is equally important for EBM process in terms of creating the CLC microstructure in TiAl alloy as this value ensures that the maximum heat flow direction remain more or less the same (i.e. along the Z-direction) regardless of 90° beam raster direction rotation between layers. In terms of sample A (CLC microstructure), a combination of beam current of 20 mA and scanning speed of 6000

mm/s were applied to achieve the optimised solidification condition with high values of $G_z/G_x$=14.1 and $G/v_n$=4.4×10$^9$ K s/m$^2$, see Fig. 4a and 4b. However, the equiaxed homogeneous microstructure (Fig. 5b, 5c and Fig. 7a to 7d) was found for samples B and C with high $G/v_n$ values of 4.1×10$^9$ K s/m$^2$ and 1.2×10$^9$ K s/m$^2$ respectively. It is very likely to attribute this phenomenon to the smaller $G_z/G_x$ value of samples B and C (7.4 for the former and 2.9 for the latter) compared to 14.1 for sample A, Fig. 4a. In sum, a small value of $G_z/G_x$ means that maintaining a consistent growth direction (i.e. along Z-direction) of prior β-phase grains in TiAl alloy is too difficult when a standard EBM beam raster scanning strategy is applied.

The much finer microstructural features in as-EBM samples B to D shown in Fig. 7a, 7c and 7e, compared to sample A, suggest the presence of successive solid-state phase transformation that could involve several times of the β→α phase transformation. Because there are 12 possible α-phase variants for the β→α phase transformation, the lamellar orientation within colonies are very difficult to be controlled, i.e. the resulting lamellar colony grains in essence comes with varying lamellar orientations for a β-solidifying TiAl alloy. This seems to be the case as even for the present sample A with the CLC microstructure, their lamellar colonies exhibited 0° and 45° orientations relative to Z-direction, Fig. 6a. These two distinct lamellar orientations are consistent with the theoretical analysis of β→α phase transformation that was performed for a β-solidifying TiAl alloy by Chen et al. [30]. Following the same research idea of Johnson et al. [31,32], it might be possible to obtain a columnar grained EBM TiAl alloy with the lamellar microstructure perpendicular to Z-direction by the addition of Si (or other equivalent elements) to shift primary α-phase region towards a much lower Al content.

The large amount of residual B2-phase (14.9% in Table 3) may suggest that prior β-phase plays a certain role in creating the CLC microstructure. It seems that B2-phase lamellae are the skeleton of the CLC microstructure particularly considering the morphology of γ lamellae (Fig. 6b) and B2 lamellae (Fig.6c). It is postulated that if the successive α→β and β→α phase transformation process arising from cyclic heat treatments does not remove completely B2-phase from the microstructure, the anchoring effect of residual B2-phase could potentially help to maintain the preferred orientation. This again highlights the importance of a tight control of EBM process parameters to achieve the desired CLC microstructure in TiAl alloy.

The product of thermal gradient and velocity, $G \times v_n$, represents the nucleation driving force during the solidification process. This essentially affects the primary dendrite arm spacing and the width of columnar colony grains. Fig. 12 shows that the values of $G \times v_n$ under the considered parameter sets ranged from $7.7 \times 10^{10}$ to $2.8 \times 10^{13}$ K/s. It can be seen that $G \times v_n$ increased monotonically with the beam current $I$, but increased initially and then decreased with $v_b$; a similar trend has been noticed for $G/v_n$ in Fig. 4b. The maximum value region for $G \times v_n$ was found to be in the range of $v_b$ from 4000 to 8000 mm/s and $I$ from 15 to 20 mA. In fact, this region overlaps with the parameter selection window for achieving the CLC microstructure in sample A. The value of $G \times v_n$ was calculated to be $2.8 \times 10^{13}$ K/s from the present numerical model. This high nucleation driving force means that obtaining a very wide columnar colony grains becomes impossible in theory for EBM TiAl alloy.

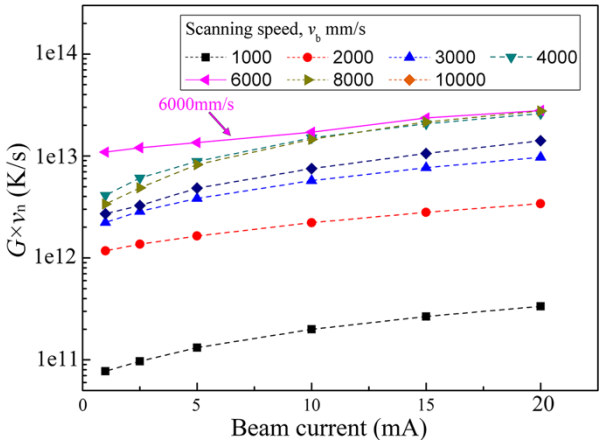


**Fig. 12.** The influence of beam current $I$ and scanning speed $v_b$ on the product of thermal gradient and velocity, $G \times v_n$.

It is also interesting to note that for such a high value of $G \times v_n$ in sample A, the pole figure of $\{10\bar{1}2\}_\alpha$ in Fig. 10f does not show the expected correlations with $\{100\}_\beta$ in Fig. 10a. On the contrary, the texture of $\{11\bar{2}0\}_\alpha$, represented by red arrows in Fig. 10e, are solely superimposed on the positions of $\{100\}_\beta$ B2-phase texture in Fig. 10a. This suggests that most of the α-phase were selectively precipitated out from the $\{11\bar{2}0\}_\alpha$ crystallographic plane. According to the classic theory in terms of crystallogprahic orentaition possibilities for α-phase nucleation and growth in TiAl alloy during the β→α phase transformation, $\{11\bar{2}0\}_\alpha$ texture should appear with a 1/3 probability while $\{10\bar{1}2\}_\alpha$ texture with a 2/3 probability [33,34]. This is obviously not the case for sample A that shows almost 100% $(11\bar{2}0)_\alpha$ texture.

This experimental finding indicates the possibility in controlling the orientation of β/α lamellae interfaces by the use of EBM process even with the very high value of $G \times v_n$.

Finally, the named near-lamellar microstructure for sample C is not a covnetionally observed TiAl microstructure produced by cast and heat treatment, considering a very low $\alpha_2$-phase content. As discussed before, the microstructural degradation associated with the high-temperature annealing during the EBM process is responsible for the resulting low $\alpha_2$-phase in sample C. However, it is still appropriate to name this microstructure with the near-lamellar, because we have collected direct TEM micrograph to evidence the lamellar characteristic of the microstructure for sample C, Fig. 13.

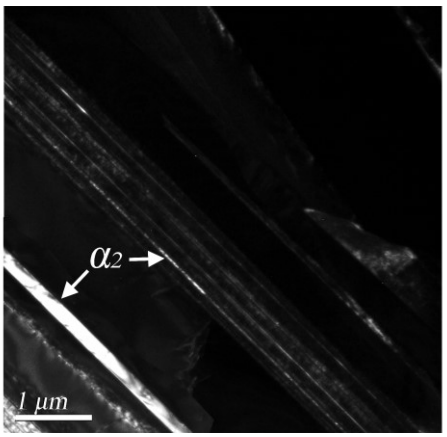


**Fig. 13.** A representive TEM dark-field micrograph of sample C showing the characteristics of lamellar structure.

## 6. Conclusions

With the tight control of both thermal gradient and velocity of solidification front, EBM of high Nb-TiAl alloy produces a highly columnar prior β grain structure within which the presence of γ/B2 lamellae and extended lamellar colonies along the Z-direction was found. The following conclusions can be reached:

1) A moderate scanning speed and large beam current is required to promote the epitaxial grain growth in EBM γ-TiAl alloy.
2) The orientation relationships as shown by pole figures of $\{0001\}_{\alpha 2}$ and $\{110\}_{\beta}$, and pole figures of $\{110\}_{\gamma}$ and $\{11\bar{2}0\}_{\alpha 2}$ indicate that both the L+β→α and α→$\alpha_2$+γ phase transformation processes are responsible for the resulting phase constitution in as-EBM sample with the columnar lamellar colony microstructure.

3) The orientation relationship between the pole figure of $\{11\bar{2}0\}_\alpha$ and $\{100\}_\beta$ is the result of geometrical symmetry requirement, which is in accordance with that in cast-TiAl. This is another clear evidence that the solidification path for EBM high Nb-TiAl alloy involves the high-temperature α-phase field.
4) The epitaxial growth of prior β grains through different layers and the anchoring effect of residual B2-phase are the most likely reasons for the formation of columnar lamellar colony structure for EBM γ-TiAl alloy.

## Acknowledgement

This work was funded by China NSFC (51831001 and 51671016) and the State Key Laboratory for Advanced Metals and Materials, USTB (2017-ZD03). Bo Chen acknowledges UK EPSRC for financial support through grants EP/P025978/1 and EP/R043973/1 to facilitate this international research collaboration. He further extends his sincere thank you to Prof. Sheng-kai Gong, Beihang University, in providing additional financial support.

## References

[1] C. Körner, Additive manufacturing of metallic components by selective electron beam melting - A review, Int. Mater. Rev. 61 (2016) 361–377. https://doi.org/10.1080/09506608.2016.1176289.

[2] E. Chauvet, C. Tassin, J. Blandin, R. Dendievel, G. Martin, Producing Ni-base superalloys single crystal by selective electron beam melting, Scr. Mater. 152 (2018) 15–19. http://dx.doi.org/10.1016/j.scriptamat.2018.03.041.

[3] N. Raghavan, R. Dehoff, S. Pannala, S. Simunovic, M. Kirka, J. Turner, N. Carlson, S.S. Babu, Numerical modeling of heat-transfer and the influence of process parameters on tailoring the grain morphology of IN718 in electron beam additive manufacturing, Acta Mater. 112 (2016) 303–314. http://dx.doi.org/10.1016/j.actamat.2016.03.063.

[4] H. Helmer, A. Bauereiß, R.F. Singer, C. Körner, Grain structure evolution in Inconel 718 during selective electron beam melting, Mater. Sci. Eng. A. 668

(2016) 180–187. http://dx.doi.org/10.1016/j.msea.2016.05.046

[5] H. Peng, Y. Shi, S. Gong, H. Guo, B. Chen, Microstructure, mechanical properties and cracking behaviour in a nickel - base superalloy fabricated by electron beam melting, Mater. Des. 159 (2018) 155–169. https://doi.org/10.1016/j.matdes.2018.08.054.

[6] S.S. Al-Bermani, M.L. Blackmore, W. Zhang, I. Todd, The origin of microstructural diversity, texture, and mechanical properties in electron beam melted Ti-6Al-4V, Metall. Mater. Trans. A. 41 (2010) 3422–3434. http://dx.doi.org/10.1007/s11661-010-0397-x.

[7] A.A. Antonysamy, J. Meyer, P.B. Prangnell, Effect of build geometry on the β -grain structure and texture in additive manufacture of Ti-6Al-4V by selective electron beam melting, Mater. Charact. 84 (2013) 153–168. https://doi.org/10.1016/j.matchar.2013.07.012.

[8] X. Tan, Y. Kok, Y.J. Tan, M. Descoins, D. Mangelinck, S.B. Tor, K.F. Leong, C.K. Chua, Graded microstructure and mechanical properties of additive manufactured Ti-6Al-4V via electron beam melting, Acta Mater. 97 (2015) 1–16. https://doi.org/10.1016/j.actamat.2015.06.036.

[9] H. Sharma, D. Parfitt, A.K. Syed, D. Wimpenny, E. Muzangaza, G. Baxter, B. Chen, A critical evaluation of the microstructural gradient along the build direction in electron beam melted Ti-6Al-4V alloy, Mater. Sci. Eng. A. 744 (2019) 182–194. http://dx.doi.org/10.1016/j.msea.2018.12.016.

[10] D. Cormier, O. Harrysson, T. Mahale, H. West, Freeform fabrication of titanium aluminide via electron beam melting using prealloyed and blended powders, Res. Lett. Mater. Sci. 34737 (2007) 1–4. http://dx.doi.org/10.1155/2007/34737.

[11] L.E. Murr, S.M. Gaytan, A. Ceylan, E. Martinez, J.L. Martinez, D.H. Hernandez, B.I. Machado, D.A. Ramirez, F. Medina, S. Collins, R.B. Wicker, Characterization of titanium aluminide alloy components fabricated by additive manufacturing using electron beam melting, Acta Mater. 58 (2010) 1887–1894. https://doi.org/10.1016/j.actamat.2009.11.032.

[12] S. Biamino, A. Penna, U. Ackelid, S. Sabbadini, O. Tassa, P. Fino, M. Pavese, P. Gennaro, C. Badini, Electron beam melting of Ti-48Al-2Cr-2Nb alloy: Microstructure and mechanical properties investigation, Intermetallics. 19 (2011) 776–781. http://dx.doi.org/10.1016/j.intermet.2010.11.017.

[13] G. Baudana, S. Biamino, B. Kloden, A. Kirchner, T. Weißg, B. Kl, B. Kieback, M. Pavese, D. Ugues, P. Fino, C. Badini, Electron beam melting of Ti-48Al-2Nb-0.7Cr-0.3Si: Feasibility investigation, Intermetallics. 73 (2016) 43–49. http://dx.doi.org/10.1016/j.intermet.2016.03.001.

[14] M. Todai, T. Nakano, T. Liu, H.Y. Yasuda, K. Hagihara, K. Cho, M. Ueda, M. Takeyama, Effect of building direction on the microstructure and tensile properties of Ti-48Al-2Cr-2Nb alloy additively manufactured by electron beam melting, Addit. Manuf. 13 (2017) 61–70. http://dx.doi.org/10.1016/j.intermet.2016.03.001.

[15] W. Kan, B. Chen, C. Jin, H. Peng, J. Lin, Microstructure and mechanical properties of a high Nb-TiAl alloy fabricated by electron beam melting, Mater. Des. 160 (2018) 611–623. https://doi.org/10.1016/j.matdes.2018.09.044.

[16] J. Schwerdtfeger, C. Körner, Selective electron beam melting of Ti-48Al-2Nb-2Cr: Microstructure and aluminium loss, Intermetallics. 49 (2014) 29–35. http://dx.doi.org/10.1016/j.intermet.2014.01.004.

[17] W. Xu, E.W. Lui, A. Pateras, M. Qian, M. Brandt, In situ tailoring microstructure in additively manufactured Ti-6Al-4V for superior mechanical performance, Acta Mater. 125 (2017) 390–400. https://doi.org/10.1016/j.actamat.2016.12.027.

[18] A. Basak, S. Das, Epitaxy and microstructure evolution in metal additive manufacturing, Annu. Rev. Mater. Res. 46 (2016) 1–25. http://dx.doi.org/10.1146/annurev-matsci-070115-031728.

[19] J. Zhang, F. Liou, W. Seufzer, K. Taminger, A coupled finite element cellular automaton model to predict thermal history and grain morphology of Ti-6Al-4V during direct metal deposition (DMD), Addit. Manuf. 11 (2016) 32–39. http://dx.doi.org/10.1016/j.addma.2016.04.004.

[20] Comsol, Heat Transfer Module Application Library Manual, Comsol Multiphysics 5.2

[21] S.P. Narra, R. Cunningham, J. Beuth, A.D. Rollett, Location specific solidification microstructure control in electron beam melting of Ti-6Al-4V, Addit. Manuf. 19 (2018) 160–166. https://doi.org/10.1016/j.addma.2017.10.003.

[22] L. Thijs, F. Verhaeghe, T. Craeghs, J. Van Humbeeck, J. Kruth, A study of the microstructural evolution during selective laser melting of Ti-6Al-4V, Acta

Mater. 58 (2010) 3303–3312. http://dx.doi.org/10.1016/j.actamat.2010.02.004.

[23] S.A. Khairallah, A.T. Anderson, A. Rubenchik, W.E. King, Laser powder-bed fusion additive manufacturing: Physics of complex melt flow and formation mechanisms of pores, spatter, and denudation zones, Acta Mater. 108 (2016) 36–45. http://dx.doi.org/10.1016/j.actamat.2016.02.014.

[24] H.M. Yang, M.H. Song, L.S. Luo, C.Y. Wang, H.Q. Qi, C. Yang, Calculation of aluminum equivalent based on Thermo-Calc software in Ti-Al-Nb ternary system, Mater. Sci. Forum. 788 (2014) 144–149. https://doi.org/10.4028/www.scientific.net/MSF.788.144.

[25] N.A. Belov, N.I. Dashkevich, S.O. Bel'tyukova, Phase composition of Al–Ti–Nb–Mo γ alloys in the heat-treatment temperature range: Calculation and experiment, Russ. Metall. 2015 (2015) 576–584. https://doi.org/10.1134/S0036029515070046.

[26] V.T. Witusiewicz, A.A. Bondar, T.Y. Velikanova, U. Hecht, The Al–B–Nb–Ti system IV. Experimental study and thermodynamic re-evaluation of the binary Al-Nb and ternary Al-Nb-Ti systems, J. Alloys Compd. 472 (2009) 133–161. https://doi.org/10.1016/j.jallcom.2008.05.008.

[27] T. Cheng, M. Loretto, The decomposition of the beta phase in Ti–44Al–8Nb and Ti–44Al–4Nb–4Zr–0.2 Si alloys, Acta Mater. 46 (1998) 4801–4819. https://doi.org/10.1016/S1359-6454(98)00113-X.

[28] W. Kan, Y. Liang, H. Peng, B. Chen, H. Guo, J. Lin, Microstructural degradation of Ti-45Al-8Nb alloy during the fabrication process by electron beam melting, JOM. 69 (2017) 2596–2601. https://doi.org/10.1016/j.matdes.2018.09.044.

[29] J. Lapin, Z. Gabalcová, Solidification behaviour of TiAl-based alloys studied by directional solidification technique, Intermetallics. 19 (2011) 797–804. http://dx.doi.org/10.1016/j.intermet.2010.11.021.

[30] G. Chen, Y. Peng, G. Zheng, Z. Qi, M. Wang, H. Yu, C. Dong, C.T. Liu, Polysynthetic twinned TiAl single crystals for high-temperature applications, Nat. Mater. 15 (2016) 876–881. https://doi.org/10.1038/NMAT4677.

[31] D.R. Johnson, H. Inui, M. Yamaguchi, Directional solidification and microstructural control of the TiAl/Ti3Al lamellar microstructure in TiAl-Si alloys, Acta Mater. 44 (1996) 2523–2535. https://doi.org/10.1016/1359-

6454(95)00338-X.

[32] D.R. Johnson, Y. Masuda, H. Inui, M. Yamaguchi, Alignment of TiAl/Ti3Al lamellar microstructure in TiAl alloys by growth from a seed material, Acta Mater. 45 (1997) 2523–2533. http://dx.doi.org/10.1016/S1359-6454(96)00335-7.

[33] M.C. Kim, M.H. Oh, J.H. Lee, H. Inui, M. Yamaguchi, D.M. Wee, Composition and growth rate effects in directionally solidified TiAl alloys, Mater. Sci. Eng. A. 239 (1997) 570–576. https://doi.org/10.1016/S0921-5093(97)00632-1.

[34] I.S. Jung, H.S. Jang, M.H. Oh, J.H. Lee, D.M. Wee, Microstructure control of TiAl alloys containing β stabilizers by directional solidification, Mater. Sci. Eng. A. 329 (2002) 13–18. https://doi.org/10.1016/S0921-5093(01)01494-0.